ADVANCED BIOLOGY
www.advanced-bio.com

Distinct Morphologies of Bone Apatite Clusters in Endochondral and Intramembranous Ossification

Emilio Satoshi Hara, Noriyuki Nagaoka, Masahiro Okada, Takayoshi Nakano, and Takuya Matsumoto**

Bone apatite crystals grow in clusters, but the microstructure of these clusters is unknown. This study compares the structural and compositional differences between bone apatite clusters formed in intramembranous (IO) and endochondral ossification (EO). Calvaria (IO) and femurs (EO) are isolated from mice at embryonic days (E) 14.5 to 15.5 and post-natal days (P) 6 to 7, respectively. Results show that the initially formed bone apatite clusters in EO (≅1.2 μm^2) are >10 times larger than those in IO (≅0.1 μm^2), without significant changes in ion composition. In IO (E14.5 calvarium), early minerals are formed inside matrix vesicles (MVs). In contrast, in EO (P6 femur epiphysis), no MVs are observed, and chondrocyte-derived plasma membrane nanofragments (PMNFs) are the nucleation site for mineralization. Apatite cluster size difference is linked with the different nucleation sites. Moreover, an alkaline pH and slow P supply into a Ca-rich microenvironment are suggested to facilitate apatite cluster growth, as demonstrated in a biomimetic mineralization system. Together, the results reveal for the first time the distinct and exquisite microstructures of bone apatite clusters in IO and EO, and provide insightful inspirations for the design of more efficient materials for bone tissue engineering and repair.

1. Introduction

Bone tissue engineering is one of the major research targets in current regenerative medicine. Bioceramics (e.g., hydroxyapatite, carbonated apatite)[1] and polymers (e.g., collagen, polylactic acid)[2] have been widely applied for this purpose. Nevertheless, these materials present limitations related to mimicking the biological and/or biomechanical properties of natural bone apatite. For instance, although hydroxyapatite-based bone mimetics present chemical similarities with natural bone, they show poor resorbability and remain in the transplanted area even after 10 years.[1] Alternative therapeutics using growth factors (e.g., bone morphogenetic protein 2 and basic fibroblast growth factor),[3] or cells, such as osteoblasts or mesenchymal stem/progenitor cells (MSCs), have also been introduced.[4] These methods, however, are costly and time-consuming, because cell therapies usually involve the transplantation of mature osteoblasts, and osteoblastic differentiation requires ≈2–3 weeks.[5]

Recent multidisciplinary approaches merging the knowledge in developmental biology with methods/techniques in tissue engineering have enabled the development of unprecedented technologies for cartilage and bone tissue engineering.[6] In this context, previous approaches for promoting bone regeneration were suboptimal as they were essentially based only on the concept of osteoblast-driven intramembranous ossification (IO).

Bone is formed through two distinct processes: IO and endochondral ossification (EO).[7] Intramembranous ossification begins inside the osteoblast-secreted extracellular vesicles, i.e., matrix vesicles (MVs), and forms the flat bones (e.g., skull) and the cortical bone.[7–9] Matrix vesicles refer to small (20–200 nm) spherical bodies transported via lysosome and secreted by exocytosis from the cells, mainly osteoblasts.[10,11] On the other hand, in EO, bone replaces a cartilage intermediate.[12] Recently, EO was shown to initiate from chondrocyte-derived plasma membrane nanofragments (PMNFs), in the absence of osteoblasts and MVs.[8,13] Previous studies have shown that the membrane and enzymes constituting MVs are different from the parent cell membrane.[14,15] On the other hand, PMNFs are direct fragments of the parent cell membrane. Thus, MVs and PMNFs could be regarded to have different composition in phospholipids and enzymes,[14,16] and could be leading to the formation of apatite clusters with different structures. However, little is known about the exact morphology of bone apatite clusters formed from MVs (IO) and PMNFs (EO).

E. S. Hara, M. Okada, T. Matsumoto
Department of Biomaterials
Okayama University Graduate School of Medicine
Dentistry and Pharmaceutical Sciences
Okayama 700-8525, Japan
E-mail: haraemilio@okayama-u.ac.jp; tmatsu@md.okayama-u.ac.jp
N. Nagaoka
Dental School
Okayama University, Advanced Research Center for Oral and Craniofacial Sciences
Okayama 700-8525, Japan
T. Nakano
Division of Materials and Manufacturing Science
Graduate School of Engineering
Osaka University
2-1, Yamadaoka, Suita-Shi, Osaka 565-0871, Japan
The ORCID identification number(s) for the author(s) of this article can be found under https://doi.org/10.1002/adbi.202200076.

DOI: 10.1002/adbi.202200076

Many studies have been carried out to identify the composition, growth, and maturation, as well as the size and orientation of bone apatite. Spherical or irregular amorphous calcium phosphate (ACP, d ≈ 50–80 nm) has been reported to be the precursors of platelet-like bone apatites.[17,18] Posner and colleagues thought that in mature bone ACP and crystalline apatite coexisted.[8,9] Several biomimetic models have been proposed to explain the crystallization of ACP to apatite and the subsequent steps of growth and maturation of bone apatite and their clusters, including the effect of ions and their osmotic equilibrium (e.g., Mg, Sr, citrate),[19,20] water molecules,[21,22] and matrix components (e.g., amino acids, collagen, polysaccharides).[23]

Numerous techniques, including electron tomography and synchrotron radiation-based X-ray tensor tomography,[24] have also been adopted to elucidate the nano- and micro-structure of apatites.[25] Evidence shows that bone apatite comprises plate-like crystals of about 100 nm in length, 20–30 nm in width, and 3–6 nm in thickness.[26] Importantly, bone apatite crystals grow in clusters, i.e., a group of euhedral crystals. The formation of these crystal clusters has been explained by the existence of pre-nucleation clusters of ACP.[18,27] However, despite the precise nanoscale measurements, the accuracy of the measurements is flawed by the low representability and generalizability of in vitro models that fail to replicate the bone tissue conditions. The bone formation mode (i.e., IO or EO), and the maturation stage of the bone tissue are also critical factors determining the morphology of bone apatite and their clusters,[28] but have been overlooked.

In this context, identification and evaluation of the first minerals formed in IO and EO are key approaches to clarify not only the nucleation sites of mineral formation but also the spatio-temporal changes in mineral growth and maturation. Previous studies have identified the first minerals in mouse cortical (calvaria) and trabecular (femur epiphysis) bones at embryonic day 14.5 (E14.5) and post-natal day 6 (P6), respectively.[9,13] In both processes, ACP has been shown to be a precursor for apatite formation. Nevertheless, the differences in the morphology of the initially formed bone apatite clusters in vivo remain obscure.

This study compared and revealed for the first time the distinct morphologies of bone apatite clusters in the initial stage of bone formation in calvarium (IO) and femur epiphysis (EO). Results showed that early bone apatite clusters in EO (P6 femur epiphysis) were ≅1.2 μm^2, significantly larger than those in IO (E14.5 calvarium, ≅0.1 μm^2). The results were also confirmed in femur diaphysis and during bone healing, where EO and IO occurs simultaneously. In vitro biomimetic mineralization assays showed that pH, and slow P supply in a Ca-rich microenvironment are important factors determining apatite cluster size.

2. Results

2.1. Comparative Analysis of Apatite Clusters in Calvaria and Femur Epiphysis

Details of the systematic and spatio-temporal investigation of the initial process of bone formation in mouse calvaria and femur epiphysis (**Figure 1**A,B) can be found elsewhere.[9,13] Briefly, calvarium and femur epiphysis were respectively isolated from embryos at E14.5 and E15.5, and from newborn P6 and P7 mice under a stereoscopic microscope. The specimens were then incubated in sodium hypochlorite for selective removal of organic matter, which allowed the direct observation of the morphologies of the initially formed bone apatite clusters formed in IO (E14.5 calvarium) and EO (P6 femur epiphysis) (Figure 1C–H). Marked differences in size and morphological structure were observed between the apatite clusters formed in IO (Figure 1C,E,G) and EO (Figure 1D,F,H). Apatite clusters constituting the initial trabecular bone in femur epiphysis were >10 times larger (surface area, on average) than those constituting the cortical bone in calvaria (Figure 1I).

Previous studies have shown the importance of divalent ion substitution in determining apatite crystal size.[13] We then performed ICP analysis, and found that the ionic compositions of the IO and EO apatite clusters were identical, except for Sr (Figure 1J,K). The molar ratios of Ca/P and Mg/Ca were in agreement with previous findings in young mouse bone minerals (Ca/P = 1.53 and Mg/Ca = 0.03, in molar ratios).[30] The relative amount of strontium in the initial apatite clusters in E14.5 calvarium (Sr/Ca = 0.00036, molar ratio) was 1.58 times higher than that of the initial apatite clusters in P6 epiphysis (Sr/Ca = 0.000228, molar ratio, Figure 1K), which was closer to the findings in mature rat and human bones (Sr/Ca ≈ 0.00028, molar ratio).[31,32] Of note, since Sr levels were substantially low, it could not be detected by EDS analysis (Figure 1L).

The ionic radius of Sr (1.13 Å) is slightly higher than that of Ca (0.99 Å), thus, the crystal lattice of Sr-substituted apatite is slightly larger.[32] The length and width of Sr-substituted apatite are also slightly increased (≈6–33%) at the nanoscale, without changes in its crystallinity.[32] On the other hand, extremely high doses of Sr-substitution (Sr/Ca ratio ≥15%) is known to dramatically decrease apatite crystal size and crystallinity.[32,33] Nevertheless, since the amount of Sr in bone apatite clusters was extremely low compared to these previous in vitro experiments,[32] and more importantly, since Sr was found to be higher in calvarial apatite clusters, which were significantly smaller than those in femur epiphysis, one could assume that Sr concentration had little or no effect on apatite cluster size. Therefore, the discrepancy in the size of apatite crystal clusters in IO and EO was not related to their ionic composition.

2.2. Comparative Analysis of Mineral Nucleation Sites in Calvaria (IO) and Femur Epiphysis (EO)

We then investigated the early biomineralization process in IO and EO in more detail. Analysis of nucleation sites in IO revealed that the initial minerals have the same size (0.1 μm^2) as the osteoblast-secreted MVs (**Figure 2**A,C,F). On the other hand, in EO, the early formed minerals (initial minerals) were also small (≈0.15 μm^2), but then grew dramatically to form large clusters of ≈1.6 μm^2 (Figure 2B,D,E,G). Initial minerals were herein defined as those initially formed inside MVs or close to PMNFs and were the precursors of apatite, i.e., they were identified to be amorphous calcium phosphate (ACP). In a later stage, these minerals would maturate and transform into apatite, meanwhile grow and fuse to each other, forming a compact structure, which

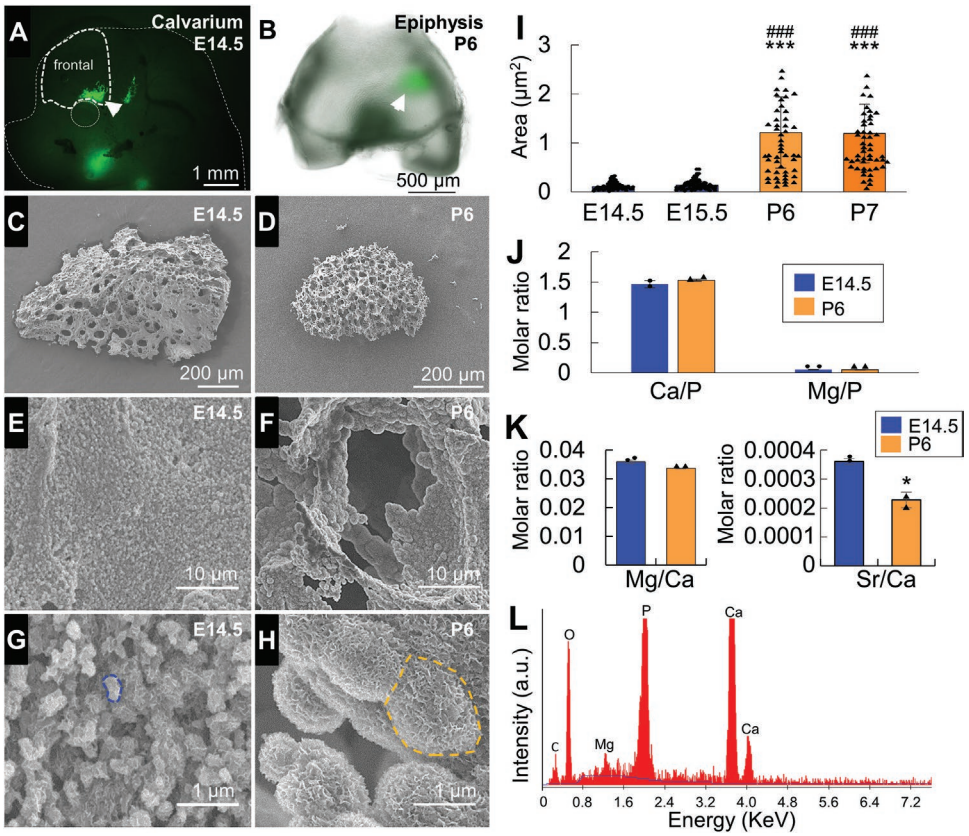

Figure 1. Distinct morphologies of initial apatite clusters in IO and EO. A,B) Calcein-labeled (green) initial mineral clusters in mouse calvarium (IO) and femur epiphysis (EO). C–H) Scanning electron microscopy (SEM) photographs of mouse calvarium (C, E, G) and epiphysis (D, F, H) after selective removal of organic matter with NaClO. I) Projection area (μm^2) of the initial bone apatite crystal clusters in calvaria (E14.5 and E15.5) and epiphyses (P6, P7). *** and ### represent $p < 0.001$, ANOVA, Tukey test, compared to E14.5 and E15.5, respectively. Data show the mean ± standard deviation (SD) of 50 apatite crystal clusters in four different samples. J,K) Comparative analysis of calcium/phosphorus (Ca/P), magnesium/phosphorus (Mg/P), magnesium/calcium (Mg/Ca), and strontium/calcium (Sr/Ca) molar ratios in the bone apatites from E14.5 calvaria and P6 femur epiphyses, estimated by inductivity coupled plasma-optical emission spectroscopy ($N = 2$/group). IO = intramembranous ossification. EO = endochondral ossification. For (K),* $p < 0.05$, Students' t-test compared to E14.5 calvaria samples. L) Representative energy dispersive spectroscopy (EDS) of the early minerals formed in P6 femur epiphysis, which was identical to that of the early minerals formed in E14.5 calvarium. Although magnesium (Mg) is clearly detectable in the EDS analysis, strontium (Sr) was undetectable.

was defined as mature minerals (Figure 2F,G). In MV-based IO, the minerals were formed inside vesicles, which may critically limit the growth of the apatite clusters. After rupture of the vesicles, the minerals could expand in size and localization throughout the collagenous matrix, but due to the high density of MVs, the radial growth of the apatite crystal clusters was also limited. On the other hand, the crystal clusters formed in PMNF-based EO could presumably grow freely in the less dense collagenous extracellular matrix (ECM, Figure 2C–E) and wider intercellular space (**Figure 3**). Details of the comparison between IO and EO, including cell size and growth speed of the entire bone are shown in **Table 1**. Figure 3 shows the cellular and ECM characteristics of the initial mineralization sites in calvarium (IO) and femur epiphysis (EO).

2.3. Comparative Analysis of Apatite Cluster Structures in Early Cortical and Trabecular Bones in Femur Diaphysis

The distinct morphologies of minerals in cortical and trabecular bones were also confirmed in femur diaphysis (primary ossification center), where EO and IO can be analyzed together. **Figure 4**A,B shows the mineralized area in femur diaphysis at E15.5. The ultrastructure of the minerals could be observed by field emission scanning electron microscope (FE-SEM) using specimens previously embedded in resin[13,29] (Figure 4C–E) or treated with NaClO for removal of organics[13] (Figure 4F). The trabecular bone is formed after the formation of the cortical bone (bone collar) (Figure 4C,D). Higher magnification images show the distinct morphologies of the early formed apatite clusters in the cortical (IO) and trabecular (EO) bones. Note that the size of apatite clusters in the cortical bone (IO) is remarkably smaller than those formed in the trabecular bone (EO).

2.4. Analysis of Environmental Calcium and pH on Mineral Cluster Growth

Previous reports showed that the cartilage extracellular environment near hypertrophic chondrocytes is substantially rich in Ca (1150 μM vs 7.44 μM inside MVs), and poor in PO_4^- (2.15 mM vs 15 mM inside MVs) compared to the enclosed microenvironment

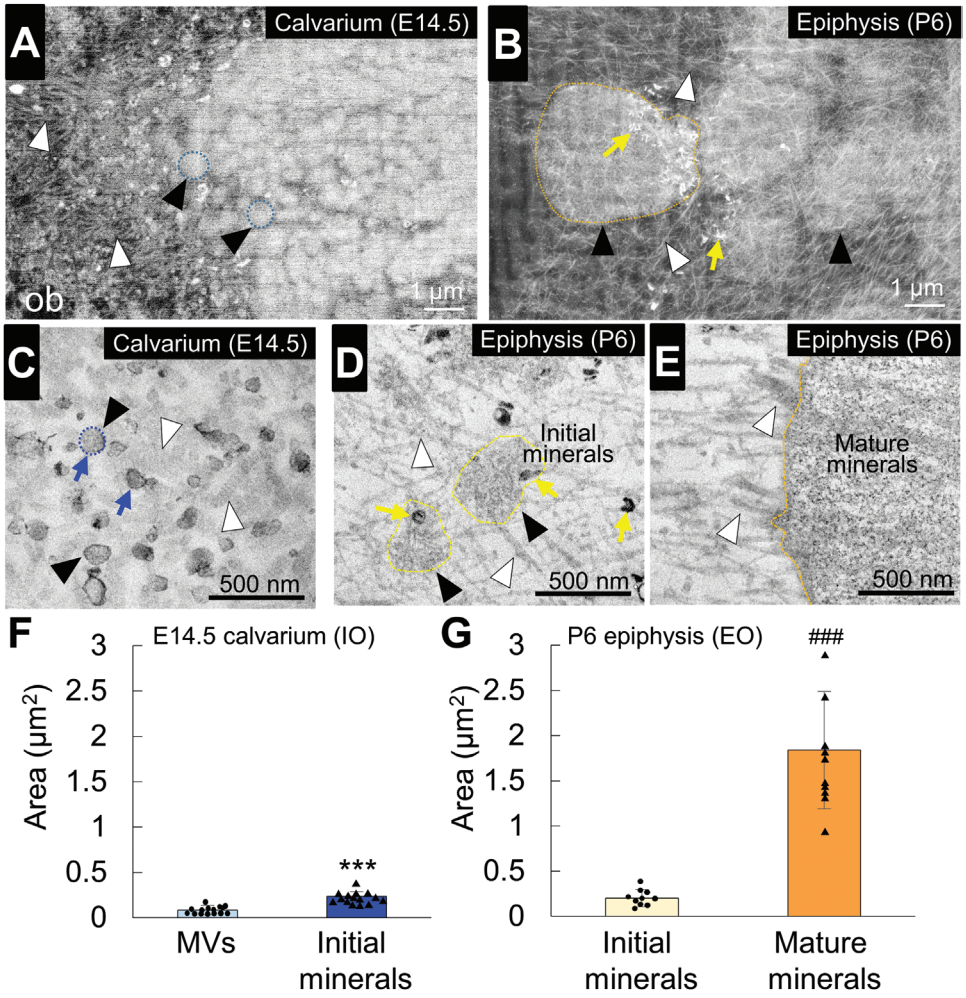

Figure 2. Nucleation sites and initial minerals in IO and EO. A,B) SEM photographs of the initial minerals taken by backscattered electron detection mode of mouse E14.5 calvarium (IO) and P6 femur epiphysis (EO) embedded in resin. C–E) Transmission electron microscope (TEM) photographs of the initial minerals and nucleation sites in IO (matrix vesicles, MVs) and EO (chondrocyte-derived plasma membrane nanofragments, PMNFs). Initial (D) and mature mineral clusters (E) in EO (femur epiphysis, P6), respectively. Projection area (μm^2) of matrix vesicles and mineral clusters formed in F) IO and G) EO calculated from FE-SEM images of resin-embedded E14.5 calvarium and P6 femur epiphysis. White arrowheads indicate collagen fibers. Black arrowheads indicate mineral clusters. Blue arrows indicate MVs. Yellow arrows indicate PMNFs (black pleomorphic material). For (F), $N = 15$ per group. For (G), $N = 10$ per group. For (A), ob = osteoblast (at the edge). For (F,G), *** and ### represent $p < 0.001$, Students' *t*-test compared to MVs (IO, E14.5 calvarium) and initial minerals (EO, P6 epiphysis), respectively. Initial minerals were defined as those formed initially inside MVs or close to PMNFs, and in a later stage, these minerals would maturate, transform into HAp, and fuse to each other, forming a compact structure, which was defined as mature minerals. IO = intramembranous ossification. EO = endochondral ossification.

inside the MVs.[34] Moreover, the pH in P6 femur epiphysis was shown to be alkaline (≈8.5).[29] An in vitro collagen diffusion system was then fabricated to mimic the in vivo conditions and evaluate the effect of pH and ion concentrations on crystal cluster growth (**Figure 5**).[29] Consistent with the in vivo findings, at pH 8.5, large apatite clusters were formed onto the small clusters deposited in the collagenous layer, whereas at pH 7.5, the crystal clusters were uniformly small (Figure 5B). Phosphate ions passed through the collagen layer and reacted with Ca in the upper chamber, where large crystal clusters were formed. This suggests that low PO_4^{-} availability in a Ca-rich alkaline environment are potential key players in the PMNF-based mineralization in EO. Of note, extended incubation time for 60 min promoted the formation of slightly larger apatite clusters with longer plate-like structures compared to those formed after 30 min (data not shown).

2.5. Comparative Analysis of Apatite Cluster Structures During Bone Healing

Bone healing in long bones is known to involve both IO and EO.[35] Thus, the morphologies of apatite crystal clusters were also evaluated in a bone healing model (**Figure 6**). Histological sections of the femurs at 0, 7, 10, and 14 days post-surgery were stained with safranin O stain for detection of cartilage matrix (Figure 6A). Cartilage in the callus was detected at days 7 and 10 of healing, but not at day 14, when the healing process was almost terminated. The minerals formed by chondrocytes in the callus (EO) showed an average size of ≈2.7 μm^2, whereas those formed by osteoblasts in the defect (IO) showed an average size of 0.380 μm^2 (Figure 6B). The minerals inside the defect grew to the same size and structure of the apatite crystal clusters of

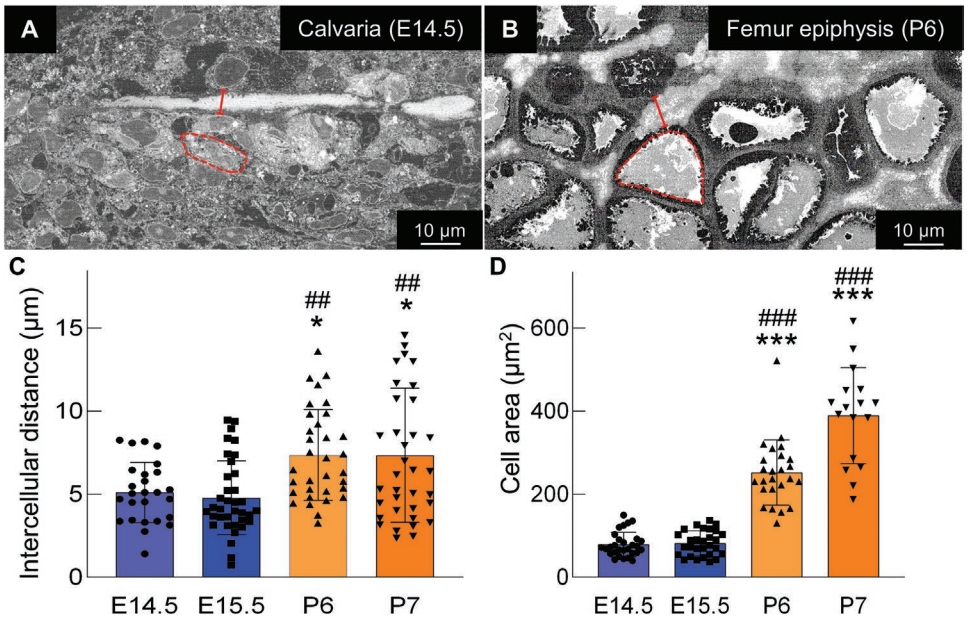

Figure 3. Cellular and extracellular matrix characteristics in mouse calvarium (IO) and femur epiphysis (EO). A,B) FE-SEM images of resin-embedded calvarium (E14.5) and epiphysis (P6). Red-dotted area shows the boundaries of cells used to determine cell projection area. Red double-arrowed line shows the intercellular distance after deposition of the initial minerals. C) Intercellular distance and D) projected area of osteoblasts (calvaria, E14.5 and E15.5) and chondrocytes (epiphysis, P6 and P7). * $p < 0.05$, *** $p < 0.001$, ANOVA, Tukey test, compared to E14.5. ## $p < 0.01$, ### $p < 0.001$, ANOVA, Tukey test, compared to E15.5. Data show the mean ± standard deviation (SD) of at least 15 areas from four different samples.

mature cortical bone (Figure 6B,C). In contrast, the apatite clusters in the callus were almost completely resorbed until day 14 of healing (Figure 6B,D).

3. Discussion

Crystal growth and maturation usually occurs in clusters and are key phenomena associated with the extraordinary mechanoproperties of bone as a biocomposite.[36] Previous reports have postulated the importance of the mineral phase, size, shape, and crystallinity of apatite crystals as determinant factors for the mechanical properties of bone tissue as predicted by composite mechanics models.[37] We herein unraveled the distinct nano- and micro-structures of bone apatite crystal clusters formed in IO and EO. In addition to the size difference, the elongated (IO) or spherical (EO) shapes of the apatite clusters would be critical factors determining the mechanoproperties of the bones. Indeed, a previous two-dimensional discrete element method (DEM) simulation showed that circular particles have the lowest, while elongated particles the highest values of peak and ultimate shear stress ratio.[38] Future in vitro and in silico studies will be necessary to shed light on the interactions between the apatite clusters and the relation between the apatite clusters and the organic matrix, including collagen fibers.

Table 1. Characteristics of the environment, nucleation site and mineral growth in intramembranous (IO) and endochondral ossification (EO).

	IO (Calvarium)	EO (Femur epiphysis)
Initial mineralization	Starts at E14.5	Starts at P6
Growth speed of the entire bone	≈95 $\mu m^3 s^{-1}$	≈46 $\mu m^3 s^{-1}$
Cell type	Osteoblasts	Chondrocytes
Cell size (projected area)	≈80 μm^2	≈250 μm^2
Matrix	Collagen type I	Collagen type II
Intercellular distance	≈5 µm	≈7 µm
Nucleation site	Matrix vesicles	Plasma membrane nanofragments
Size (projected area) of bone apatite crystal clusters	≈0.1 μm^2	≈1.6 μm^2

IO = Intramembranous ossification; EO = Endochondral ossification.

The roles of divalent ion substitution (Mg, Sr) of Ca on apatite crystal growth and cluster morphology have been largely studied.[21,30,31] Synthetic Mg-substituted apatite showed a smaller size, possibly associated with the smaller ionic radius of Mg compared to Ca. Magnesium on the apatite surface is also known to retard crystal growth, while the incorporated Mg becomes inert.[20] On the other hand, Sr, which has a larger ionic radius than Ca, induced no change in the apatite crystal size at low concentrations.[32] At high concentrations, however, Sr promoted a marked decrease in crystal size.[39] In vivo analysis of biological apatite crystal clusters formed in mice fed with an Mg-containing diet showed that they were also smaller than their counterparts without Mg. This could be due to not only the difference in ionic radius, but also in part due to the presence of strongly H-bonded intermediate water, which could reduce the water dynamics, ionic solute diffusion and chemical reactions around the apatite surfaces, and delay crystal growth.[21] However, apatite crystals grow in clusters. Herein, we found that the structural difference between the apatite

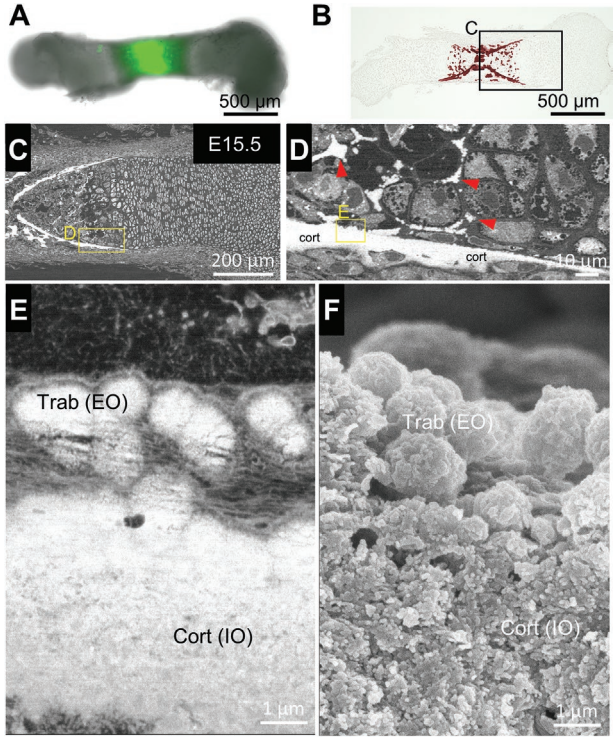

Figure 4. Distinct morphologies of trabecular (EO) and cortical (IO) bones in femur diaphysis. A) Microscopic photograph of E15.5 femur showing the calcein-labeled (green) mineralized area in the diaphysis. B) Histological section of E15.5 femur stained with alizarin red S showing the mineralized area in the diaphysis. Square represent the area shown in (C). FE-SEM photographs of the minerals in the trabecular (EO) and cortical (IO) bones taken by C–E) backscattered electron or F) secondary electron detection mode. Squares in (C) and (D) represent the area shown in (D) and (E), respectively. For (F), samples were treated with NaClO for selective removal of organic matter. The apatite crystal clusters in the trabecular bone (Trab, EO) are markedly larger than those in the cortical bone (Cort, IO). IO = intramembranous ossification. EO = endochondral ossification. Images are representative of 2 different samples.

clusters in IO and EO were not related to ionic composition, but more strongly related with the different nucleation sites in these processes, namely MVs in IO and PMNFs in EO.[9,13]

Calvarial bone begins with the migration of precursor stem cells derived from cranial neural crest cells into the frontal bone primordium at E11.5, followed by apical migration at E13.5.[40] The mesenchymal cells in the initial condensation then differentiate into osteoblasts, which then secrete collagen and release large amounts of MVs.[9,40] Thus, IO starts E14.5 inside the MVs embedded in a dense collagenous matrix secreted by osteoblasts. The confined environment inside the MVs containing nucleation factors may restrict the crystal cluster growth to small minerals. In the subsequent steps, the shortage in P and Ca ions inside the MVs may also impede further growth of the apatite crystal clusters. Furthermore, MVs are secreted in high amounts and density, therefore, after MV rupture, there would have not much space for crystal cluster growth in the collagen type I-dense ECMs (**Figure 7**).

In contrast, EO begins with the condensation of mesenchymal cells, which differentiate into chondrocytes and form the cartilaginous anlagen.[41] At E14.5, chondrocytes in the diaphysis become hypertrophic and undergo apoptosis or burst, and initiates the formation of early trabecular bone.[41,42] In post-natal days, chondrocytes in the epiphysis become hypertrophic around P5 and initial mineralization is observed at P6.[13] The very initial minerals (i.e., amorphous calcium phosphate) in EO were formed near the PMNFs,[13] and not in a closed microenvironment inside the MVs.[10] Moreover, the microenvironmental pH in P6 femur epiphysis was shown to be alkaline (pH ≅ 8.5), which facilitated the formation of spherical minerals.[29] Furthermore, after burst, chondrocytes shrink and the ECM expands toward the space previously occupied by the cells. Consequently, the ECM becomes less dense, facilitating the growth of large apatite crystal clusters within the diffused collagen type II fibers.

The in vitro biomimetic mineralization attempted to replicate the mineralization in EO. The collagen gel diffusion system allowed the analysis of the slow supply of P into a Ca-rich environment in an alkaline pH. The results indicated that these two conditions were critical to facilitate the deposition of calcium phosphate onto pre-existing minerals and promote the radial growth of apatite crystal clusters, instead of promoting the formation of nucleation sites. The slow supply of P would also limit the growth speed of apatite crystal clusters, which is supported by the in vivo findings (Table 1). Oppositely, in vitro experiments inducing rapid P reaction with Ca, i.e., immediate reaction of P and C solutions, did not promote the formation of spherical nor large apatite clusters (data not shown).

The size of apatite clusters is of fundamental importance in guiding cellular activities. Previous reports have demonstrated that micro-structured apatite markedly promoted osteoclast formation and function, as demonstrated by enhanced cell fusion and differentiation, i.e., expression of osteoclast specific proteins associated with increased tartrate-resistant acid phosphatase (TRAP) and resorption activities, compared to nano-structured counterparts.[39,43] The decreased crystal size has also been associated with an increase in surface area, porosity and hydrophilicity, which may drive the cellular responses through diverse intracellular signaling pathways.[39,43] During bone resorption, osteoclasts form a specialized, actin-rich adhesive "sealing zone." The level of surface roughness was shown to have critical effects on the formation and stability of the actin-dependent sealing zone.[44] Less-defined actin rings were detected in osteoclasts cultured onto micro-sized apatite.[39] This indicates that mechanotransduction-associated signaling molecules, including integrin, focal adhesion and YAP-TAZ, are also intensively activated by the different apatite micro-structures.[45]

The osteoconductivity of calcium phosphate bioceramics may also vary according to its composition and structure. In contrast to the findings with hydroxyapatite, nano-structured beta-tricalcium phosphate was shown to have high osteoinductivity via inducing the differentiation of large and active osteoclasts that secrete osteogenic factors, such as BMPs that facilitate the differentiation of MSCs into osteoblasts.[46] These data suggest that apatite clusters could be important extracellular signaling factors priming bone remodeling. For instance, as shown in the bone healing model, the micro-size

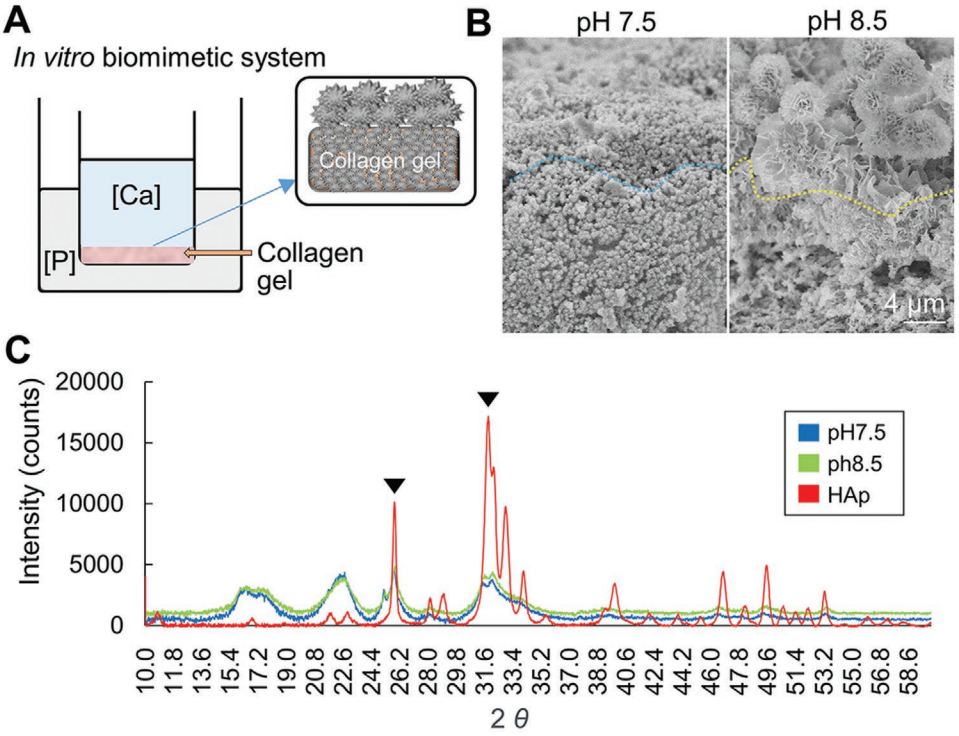

Figure 5. Biomimetic mineralization in vitro. A) Schematic illustration of the collagen gel diffusion system. B) SEM photographs of the minerals formed at pH 7.5 or 8.5 taken by secondary electron detection mode. Large apatite crystal clusters were formed onto the layer of small clusters at pH 8.5 only. C) XRD analysis of the minerals formed at pH 7.5 and 8.5. (B) and (C) are representative data from 3 different samples. The mineral products were identified to be apatite, and show low crystallinity. Commercially available HAp was used as a control.

apatite clusters formed in the callus by chondrocytes (EO) during days 7 to 10 of healing were rapidly resorbed. On the other hand, the nano-structured apatite clusters formed in the calvarium, cortical bone or inside the defect during bone healing by osteoblasts (IO) were not resorbed, but grew and reach all the same size and morphology, forming a compact and resistant bone structure. These findings suggest that cartilage matrix, including the minerals formed by chondrocytes is transient during either tissue development or healing, while the mineralized bone matrix formed by osteoblasts is less susceptible to undergo remodeling and more likely fated to be permanent. A more detailed investigation of the mechano-biophysical and biochemical factors and related signaling pathways are necessary to clarify the exact roles of apatite cluster size difference in regulating the function of osteoclasts, osteoblasts and MSCs during bone formation or bone healing.

4. Conclusion

In summary, this study revealed for the first time the distinct morphologies of bone apatite crystal clusters in the initial stages of IO and EO, and their association with the roles of MVs and PMNFs as nucleation sites for mineral formation in IO and EO, respectively. These results provide a fundamental understanding of the process and mechanisms of bone mineral cluster formation and growth, and inspirations for the design of novel biofunctional materials.

5. Experimental Section

Animals: Pregnant Institute of Cancer Research (ICR) mice were purchased from Shimizu Laboratory Supplies Co. Ltd. (Kyoto, Japan). Embryonic mice at day E14.5 to E15.5 or newborn mice at post-natal day 6 (P6) and P7 were used in the experiments according to the Guidelines for Animal Research of Okayama University. The Animal Care and Use Committee of Okayama University approved the research protocols (OKU-2014283 and OKU-2015542).

Calcein (20 mg kg^{-1}) was injected into pregnant or newborn mice for identification of the initial minerals in calvaria and femur epiphysis, one day before euthanasia.[9] Embryos at E14.5 or femur epiphysis from P6 neonatal mice were collected and observed under a fluorescence stereoscopic microscope (SZX12, Olympus, Tokyo, Japan), available at the Central Research Laboratory, Okayama University Medical School.

For analysis of bone healing, femur defects were made with a round steel bur (1 mm) using a handpiece micromotor in 6-week-old ICR female mice. Femurs were collected at 7, 10, and 14 days post-surgery for histological analysis. Alternatively, the samples were treated with NaClO for removal of the organic matter before electron microscopic observation.

Field Emission Scanning Electron Microscope (FE-SEM), Energy Dispersive X-ray Spectroscopy (EDS), and Transmission Electron Microscope (TEM): For analysis of the microstructure and elemental composition of apatite clusters, freshly harvested calvaria (E14.5, E15.5), and epiphyses (P6, P7) were maintained in NaClO (FUJIFILM Wako Pure Chemical Industries, Osaka, Japan) to remove organic matter for at least 24 h. The samples were then thoroughly washed with pure water and dehydrated with ethanol. The samples were placed onto an aluminum holder and submitted to osmium coating (Neoc-STB, Meiwafosis, Tokyo, Japan) before observation using a FE-SEM (JSM-6701F, JEOL) equipped with an EDS detector (EDAX, Mahwah, NJ, USA).

For analysis of the spatiotemporal localization of early mineral clusters in the extracellular matrix, femurs (E14.6, E15.5), and epiphyses (P6) were fixed in 2% glutaraldehyde/2% paraformaldehyde (PFA)

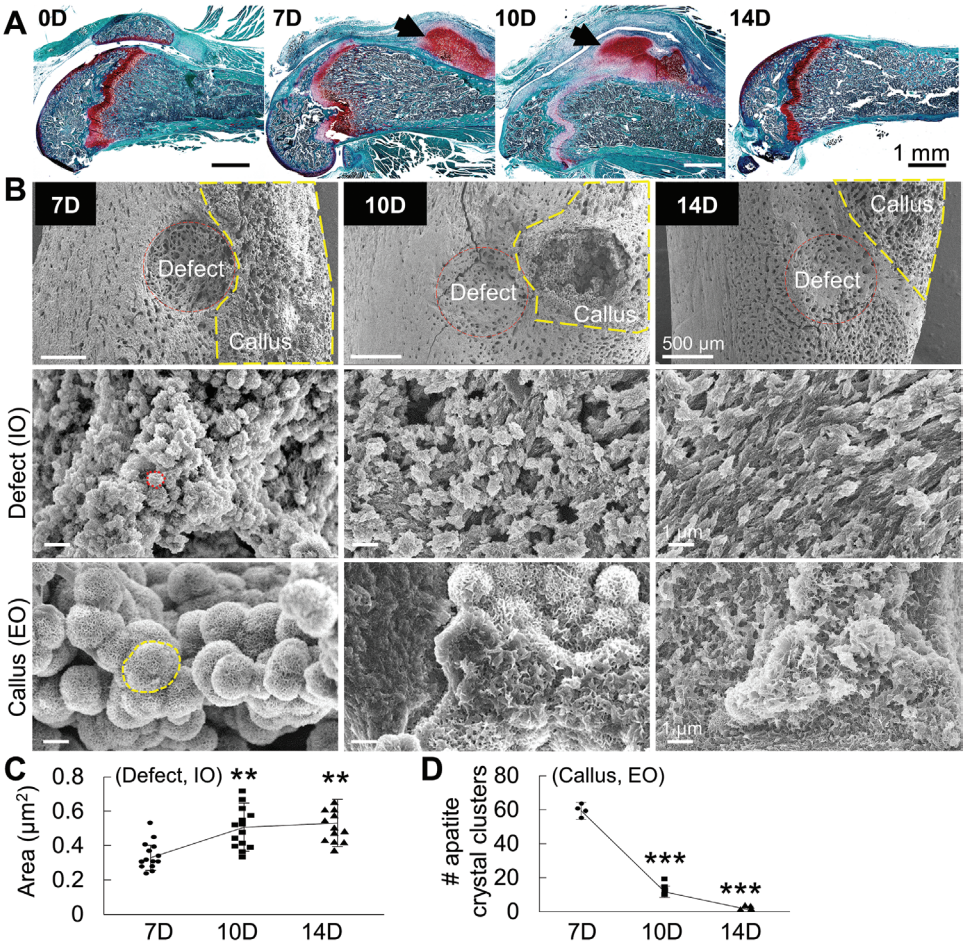

Figure 6. Analysis of apatite crystal cluster size during bone healing. A) Fast green/safranin O stained sections of adult mouse femurs at 0, 7, 10, and 14 days after the surgical defect. Arrows indicate the cartilaginous tissue (callus, EO) during bone healing at days 7 and 10 post-surgery. B) SEM photographs taken by secondary electron detection mode of the defect and callus regions in femurs after 7, 10, and 14 days of surgery, after treatment with NaClO. Upper panel: lower magnification images. Red-dotted area shows the defect region. Yellow-dotted area shows the callus region. Middle and Lower panels: High magnification images of the minerals inside the defect area (IO, middle panel) and callus (EO, lower panel). C) Projected area of crystal clusters within the defect (IO) during bone healing. $N = 15$, from four areas in 2 different samples. D) Number of apatite crystal clusters per 110 μm^2 within the callus (EO). $N = 4$ per group, from four areas in 2 different samples. D = days. IO = intramembranous ossification. EO = endochondral ossification. ** $p < 0.01$, *** $p < 0.001$, ANOVA, Tukey test, compared to 7D, respectively.

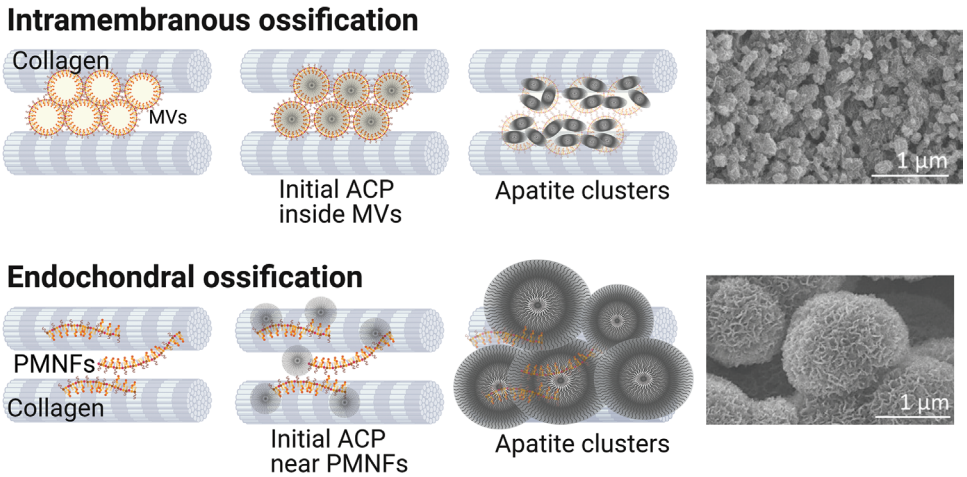

Figure 7. Proposed schematic design of the model of IO and EO with the roles of MVs and PMNFs in mineral formation and the characteristics of apatite clusters formed in IO and EO.

solution and embedded in resin, as reported.[13] In brief, fixed specimens were washed with phosphate-buffered saline (PBS), and incubated in 3% potassium ferrocyanide (Sigma-Aldrich, St. Louis, MO, USA) 2% osmium tetroxide (TAAB Laboratories Equipment Ltd., Berkshire, UK) for 1 h on ice. Samples were then washed thoroughly and incubated with freshly prepared 1% thiocarbohydrazide (Sigma-Aldrich) for 20 min at room temperature (RT). Tissues were washed thoroughly and incubated with 1% osmium for 30 min at RT. Samples were washed, dehydrated with ethanol and propylene oxide, and embedded in EPON 812 resin (TAAB Laboratories Equipment Ltd.). Specimen were then polished and cross-sectioned by an argon ion etching (SM-090101 Cross Section Polisher; JEOL, Tokyo, Japan) and observed with FE-SEM in backscattered electron detection mode (5 kV, 20 μA).[13]

Resin-embedded calvaria (E14.5) and epiphysis (P6) were sectioned with a diamond knife (80 nm) and placed on grids for observation in a transmission electron microscope (TEM; JEM-2100, JEOL).

Histological Analysis: Freshly isolated femurs (E15.5) were immediately embedded in cryomedium and frozen. Cryosections (7 μm, CM3050S Leica Microsystems, Wetzlar, Germany) were fixed in 4% PFA and stained with alizarin red S stain for detection of the mineralized area.

Femurs submitted to surgical defects were fixed in 4% PFA and embedded in paraffin, as reported.[13] Sections (5 μm, HM340E Thermo Fisher Scientific, Waltham, MA, USA) were stained with fast green/safranin O stain for detection cartilage matrix. Images were taken with a fluorescence microscope (Biozero BZ-X700, Keyence, Osaka, Japan).

Inductivity Coupled Plasma-Optical Emission Spectroscopy (ICP-OES): Dried bone apatite (2 mg) obtained after NaClO treatment of calvaria (E14.5) or femur epiphyses (P6) were dissolved in 0.1 M HNO_3 and submitted to quantitative analysis of phosphate, calcium, strontium, and magnesium ions by using ICP-OES (VISTA-PRO, Seiko Instruments, Chiba, Japan). Due to the small size of the specimens, ≈12 embryos or newborn mice were used to obtain 2 mg of dried bone apatite. The experiment was performed with two independent samples per group.

Biomimetic Mineralization In Vitro: The biomimetic mineralization was performed in a gel diffusion system comprising a collagen gel in between calcium ($CaCl_2$, 100 mM) and phosphate (PBS, 100 mM) solutions.[29]

The collagen gel was prepared by mixing type I collagen (3 mg mL^{-1}, Cellmatrix type I-A, Nitta Gelatin Inc., Osaka, Japan) with a neutralizing buffer (0.05 N NaOH/2.2% $NaHCO_3$/200 mM 4-(2-hydroxyethyl)-1-piperazineethanesulfonic acid, HEPES). The gel was immediately poured onto a filter strainer (70 μm) and incubated at 37 °C for 30 min until complete gelation. Calcium and phosphate solutions, previously adjusted to pH 7.5 and 8.5, were poured into the opposite sides of the collagen gel in a 6-well plate. The reaction was maintained for 30 min. The filter strainer containing the gel was then washed, fixed in 4% PFA, dehydrated in ethanol and *t*-butanol and freeze-dried. The minerals formed in the center of the gel were observed by an FE-SEM or analyzed by X-ray diffraction.

X-Ray Diffraction (XRD): Mineralization products formed in the gel diffusion system were thoroughly washed with Milli-Q ultrapure water 3 times, 30 min each, and freeze-dried. The specimens (thin films) were then fixed onto a glass plate and analyzed using a SmartLab instrument (Rigaku Corp., Tokyo, Japan) at 40 kV and 30 mA, with 0.02° steps at 3° min^{-1} speed. Analyses were performed with triplicate samples. Commercially available hydroxyapatite (HAp) was used as the reference sample.

Image Analysis: Image analyses were performed with ImageJ (NIH, Bethesda, MD, USA). The projection areas of MVs, apatite clusters, and cells were determined by manual delineation of their boundaries. The intercellular distance was determined by the shortest distance between two adjacent cells.

Statistical Analysis: Analysis of the differences between groups was performed with unpaired Student's *t*-test (2 samples) or one-way ANOVA followed by a Tukey post-hoc correction test when comparing 3 or more samples. Prism 9 software (GraphPad Software, La Jolla, CA, USA) was used for the analyses.

Acknowledgements

The authors thank Dr. Yosuke Kunitomi for his help in the analysis of calvarial bone development. The authors also thank the Central Research Laboratory, Okayama University Medical School, where fluorescence and electron microscopes were available. This study was supported by JSPS KAKENHI Grant Numbers JP18H05254, JP19H03837, JP20H04534, and JP22H03274. The XRD experiment using SmartLab was performed at the Joint Research Center for Environmentally Conscious Technologies in Materials Science (Grant No. JPMXP0621467974) at ZAIKEN, Waseda University.

Conflict of Interest

The authors declare no conflict of interest.

Data Availability Statement

The data that support the findings of this study are available from the corresponding author upon reasonable request.

Keywords

biomineralization, bone apatite, bone callus, bone defects, endochondral ossification, intramembranous ossification

Received: March 18, 2022
Revised: June 27, 2022
Published online:

[1] K. Hayashi, R. Kishida, A. Tsuchiya, K. Ishikawa, *Mater. Today Bio* **2019**, *4*, 100031.
[2] D. G. Petre, S. C. G. Leeuwenburgh, *Tissue Eng. Part B Rev.* **2022**, *28*, 141.
[3] a) M. Ono, W. Sonoyama, K. Nema, E. S. Hara, Y. Oida, H. T. Pham, K. Yamamoto, K. Hirota, K. Sugama, W. Sebald, T. Kuboki, *Cells Tissues Organs* **2013**, *198*, 367; b) S. Nosho, I. Tosa, M. Ono, E. A.-O. Hara, K. Ishibashi, A. Mikai, Y. Tanaka, A. Kimura-Ono, T. Komori, K. Maekawa, T. A.-O. Kuboki, T. A.-O. Oohashi.
[4] Z. A.-O. X. Johnson, Y. Yuan, X. Li, T. Jashashvili, M. Jamieson, M. Urata, Y. Chen, Y. A.-O. Chai, J. A. Shibli, B. E. Nagay, L. J. Suarez, C. Urdaniga Hung, M. Bertolini, V. A. R. Barao, J. G. S. Souza, *Tissue Eng., Part C* **2022**, *28*, 179.
[5] T. Eguchi, K. Watanabe, E. S. Hara, M. Ono, T. Kuboki, S. K. Calderwood, *PLoS One* **2013**, *8*, e58796.
[6] a) R. S. Marcucio, L. Qin, E. Alsberg, J. D. Boerckel, *J. Orthop. Res.* **2017**, *35*, 2356; b) E. S. Hara, M. Okada, N. Nagaoka, T. Nakano, T. Matsumoto, *Tissue Eng., Part B* **2022**, *28*, 246.
[7] S. F. Gilbert, in *Developmental Biology*, 6th ed., Sinauer Associates, c2000, Sunderland, Mass **2000**.
[8] B. K. Hall, in *Bones and Cartilage*, 2nd ed. (Ed: B. K. Hall), Academic Press, San Diego **2015**, p. 17.
[9] Y. Kunitomi, E. S. Hara, M. Okada, N. Nagaoka, T. Kuboki, T. Nakano, H. Kamioka, T. Matsumoto, *J. Biomed. Mater. Res., Part A* **2019**, *107*, 1021.
[10] T. Iwayama, T. Okada, T. Ueda, K. Tomita, S. Matsumoto, M. Takedachi, S. Wakisaka, T. Noda, T. Ogura, T. Okano, P. Fratzl, T. Ogura, S. Murakami, *Sci. Adv.* **2019**, *5*, 0672.
[11] E. E. Golub, *Biochim. Biophys. Acta* **2009**, *1790*, 1592.
[12] P. A. Lu Valle, *Curr. Opin. Orthop.* **1993**, *4*, 85.

[13] E. S. Hara, M. Okada, N. Nagaoka, T. Hattori, T. Kuboki, T. Nakano, T. Matsumoto, *ACS Biomater. Sci. Eng.* **2018**, *4*, 617.
[14] R. E. Wuthier, *Fed. Proc.* **1976**, *35*, 117.
[15] a) S. Y. Ali, *Fed. Proc.* **1976**, *35*, 135; b) R. J. Majeska, R. E. Wuthier, *Biochim. Biophys. Acta* **1975**, *391*, 51.
[16] S. Y. Ali, *Bone Miner.* **1992**, *17*, 168.
[17] a) E. D. Eanes, I. H. Gillessen, A. S. Posner, *Nature* **1965**, *208*, 365; b) F. Betts, A. S. Posner, *Mater. Res. Bull.* **1974**, *9*, 353; c) L. Wang, G. H. Nancollas, *Chem. Rev.* **2008**, *108*, 4628; d) J. Mahamid, B. Aichmayer, E. Shimoni, R. Ziblat, C. Li, S. Siegel, O. Paris, P. Fratzl, S. Weiner, L. Addadi, *Proc. Natl. Acad. Sci. U. S. A.* **2010**, *107*, 6316; e) L.-W. Du, S. Bian, B.-D. Gou, Y. Jiang, J. Huang, Y.-X. Gao, Y.-D. Zhao, W. Wen, T.-L. Zhang, K. Wang, *Cryst. Growth Des.* **2013**, *13*, 3103.
[18] A. Lotsari, A. K. Rajasekharan, M. Halvarsson, M. Andersson, *Nat. Commun.* **2018**, *9*, 4170.
[19] a) B. Xie, G. H. Nancollas, *Proc. Natl. Acad. Sci. U. S. A.* **2010**, *107*, 22369; b) P. G. Koutsoukos, G. H. Nancollas, *J. Phys. Chem.* **1981**, *85*, 2403; c) L.-n. Niu, S. E. Jee, K. Jiao, L. Tonggu, M. Li, L. Wang, Y.-d. Yang, J.-h. Bian, L. Breschi, S. S. Jang, J.-h. Chen, David H. Pashley, Franklin R. Tay, *Nat. Mater.* **2017**, *16*, 370.
[20] H. Ding, H. Pan, X. Xu, R. Tang, *Cryst. Growth Des.* **2014**, *14*, 763.
[21] M. Okada, E. S. Hara, D. Kobayashi, S. Kai, K. Ogura, M. Tanaka, T. Matsumoto, *ACS Appl. Bio Mater.* **2019**, *2*, 981.
[22] Y. Wang, S. Von Euw, F. M. Fernandes, S. Cassaignon, M. Selmane, G. Laurent, G. Pehau-Arnaudet, C. Coelho, L. Bonhomme-Coury, M.-M. Giraud-Guille, F. Babonneau, T. Azaïs, N. Nassif, *Nat. Mater.* **2013**, *12*, 1144.
[23] a) T. Matsumoto, M. Okazaki, M. Inoue, Y. Hamada, M. Taira, J. Takahashi, *Biomaterials* **2002**, *23*, 2241; b) M. Tavafoghi, M. Cerruti, *J. R. Soc., Interface* **2016**, 13; c) F. Nudelman, K. Pieterse, A. George, P. H. Bomans, H. Friedrich, L. J. Brylka, P. A. Hilbers, G. de With, N. A. Sommerdijk, *Nat. Mater.* **2010**, *9*, 1004; d) W. Fang, H. Zhang, J. Yin, B. Yang, Y. Zhang, J. Li, F. Yao, *Cryst. Growth Des.* **2016**, *16*, 1247.
[24] M. Mastrogiacomo, G. Campi, R. Cancedda, A. Cedola, *Acta Biomater.* **2019**, *89*, 33.
[25] T. A. Grunewald, M. Liebi, N. K. Wittig, A. Johannes, T. Sikjaer, L. Rejnmark, Z. Gao, M. Rosenthal, M. Guizar-Sicairos, H. Birkedal, M. Burghammer, *Sci. Adv.* **2020**, *6*, 4171.
[26] a) P. Fratzl, M. Groschner, G. Vogl, H. Plenk Jr., J. Eschberger, N. Fratzl-Zelman, K. Koller, K. Klaushofer, *J. Bone Miner. Res.* **1992**, *7*, 329; b) N. Reznikov, M. Bilton, L. Lari, M. M. Stevens, R. Kroger, *Science* **2018**, 360; c) A. S. Posner, F. Betts, *Acc. Chem. Res.* **1975**, *8*, 273; d) R. A. Robinson, *J. Bone Jt. Surg., Am. Vol.* **1952**, *34-A*, 389.
[27] a) W. J. E. M. Habraken, J. Tao, L. J. Brylka, H. Friedrich, L. Bertinetti, A. S. Schenk, A. Verch, V. Dmitrovic, P. H. H. Bomans, P. M. Frederik, J. Laven, P. van der Schoot, B. Aichmayer, G. de With, J. J. DeYoreo, N. A. J. M. Sommerdijk, *Nat. Commun.* **2013**, *4*, 1507; b) A. Dey, P. H. H. Bomans, F. A. Müller, J. Will, P. M. Frederik, G. de With, N. A. J. M. Sommerdijk, *Nat. Mater.* **2010**, *9*, 1010.
[28] X. Su, K. Sun, F. Z. Cui, W. J. Landis, *Bone* **2003**, *32*, 150.
[29] E. S. Hara, M. Okada, T. Kuboki, T. Nakano, T. Matsumoto, *J. Mater. Chem. B* **2018**, *6*, 6153.
[30] P. J. Marie, R. Travers, E. E. Delvin, *Calcif. Tissue Int.* **1983**, *35*, 755.
[31] Y. K. Tanaka, N. Yajima, M. Okada, T. Matsumoto, Y. Higuchi, S. Miyazaki, H. Yamato, T. Hirata, *Analyst* **2017**, *142*, 4265.
[32] Z. Y. Li, W. M. Lam, C. Yang, B. Xu, G. X. Ni, S. A. Abbah, K. M. Cheung, K. D. Luk, W. W. Lu, *Biomaterials* **2007**, *28*, 1452.
[33] J. Christoffersen, M. R. Christoffersen, N. Kolthoff, O. Barenholdt, *Bone* **1997**, *20*, 47.
[34] R. E. Wuthier, G. F. Lipscomb, *Front. Biosci. - Landmark* **2011**, *16*, 2812.
[35] T. A. Einhorn, *J. Orthop. Trauma* **2005**, 19.
[36] M. Eder, S. Amini, P. Fratzl, *Science* **2018**, *362*, 543.
[37] J. S. Yerramshetty, O. Akkus, *Bone* **2008**, *42*, 476.
[38] J. Q. Tian, E. L. Liu, L. Jiang, X. Q. Jiang, Y. Sun, R. Xu, *Cr. Mec.* **2018**, *346*, 460.
[39] F. Chen, M. Wang, J. Wang, X. Chen, X. Li, Y. Xiao, X. Zhang, *J. Mater. Chem. B* **2019**, *7*, 7574.
[40] Y. Jiang, S. Zhang, C. Mao, Y. Lai, D. Wu, H. Zhao, C. Liao, W. Chen, *Int. J. Oral Sci.* **2019**, *11*, 3.
[41] B. R. Olsen, A. M. Reginato, W. Wang, *Annu. Rev. Cell Dev. Biol.* **2000**, *16*, 191.
[42] E. S. Hara, M. Okada, N. Nagaoka, T. Hattori, L. M. Iida, T. Kuboki, T. Nakano, T. Matsumoto, *Integr. Biol.* **2018**, *10*, 57.
[43] J. Costa-Rodrigues, S. Carmo, I. P. Perpetuo, F. J. Monteiro, M. H. Fernandes, *Biochim. Biophys. Acta* **2016**, *1860*, 825.
[44] D. Geblinger, L. Addadi, B. Geiger, *J. Cell Sci.* **2010**, *123*, 1503.
[45] a) A. Liedert, D. Kaspar, P. Augat, A. Ignatius, L. Claes, in *Mechanosensitivity in Cells and Tissues* (Eds: A. Kamkin, I. Kiseleva), Academia, Moscow **2005**; b) I. P. Geoghegan, D. A. Hoey, L. M. McNamara, *Curr. Osteoporos. Rep.* **2019**, *17*, 195; c) Z. Sun, S. S. Guo, R. Fassler, *J. Cell Biol.* **2016**, *215*, 445.
[46] N. L. Davison, X. Luo, T. Schoenmaker, V. Everts, H. Yuan, F. Barrere-de Groot, J. D. de Bruijn, *Eur. Cells Mater.* **2014**, *27*, 281.